European Congress on Computational Methods in Applied Sciences and Engineering
ECCOMAS Computational Fluid Dynamics Conference 2001
Swansea, Wales, UK, 4-7 September 2001

DEVELOPMENT AND APPLICATION OF A NEW WALL FUNCTION FOR COMPLEX TURBULENT FLOWS

T. J. Craft, S. E. Gant, H. Iacovides, and B. E. Launder

Department of Mechanical Engineering,
University of Manchester Institute of Science and Technology (UMIST),
PO Box 88, Manchester, M60 1QD, UK
e-mail: simon.gant@umist.ac.uk
web page: http://cfd.me.umist.ac.uk/

Key words: Wall function, RANS, turbulence modelling, eddy-viscosity models, impinging jet, CFD

Abstract. *Wall functions are widely used in commercial CFD software and offer significant savings in computational expense compared to low-Reynolds-number formulations. However, existing wall functions are based on assumed near-wall profiles of velocity, turbulence parameters and temperature which are inapplicable in complex, non-equilibrium flows. A new wall function has therefore been developed in which, instead of assuming profiles of the dependent variables, these quantities are determined by solving boundary-layer-type transport equations across a locally-defined subgrid. The new wall function has been applied to a simple channel flow and an axisymmetric impinging jet using linear and non-linear $k-\varepsilon$ turbulence models. While computational costs with this new approach are up to 60 percent higher than for standard wall functions, they are still an order of magnitude less than low-Reynolds-number calculations for the impinging jet. The results show a clear improvement in reproducing low-Re predictions over standard wall-function treatments.*

1 INTRODUCTION

The most accurate route for computing the near-wall behaviour of complex turbulent flows, using Reynolds-averaged Navier-Stokes equations, is to employ a "low-Reynolds-number" model, i.e. a model that is applicable right across the viscosity-affected sublayer to the wall itself. This requires a very fine mesh in the viscous sublayer to resolve the abrupt changes in near-wall turbulence parameters. As a consequence of the large number of computational grid cells and the slow convergence associated with the highly elongated near-wall cells, this approach leads to considerable computing times and cannot currently be used routinely in the computation of industrially-relevant three-dimensional flows.

An alternative approach is available which uses a coarser grid with large near-wall cells that span the viscous sublayer. Within the cell next to the wall empirically-derived "wall functions" are employed and in the main region of the flow domain "high-Reynolds-number" transport equations are solved. This approach offers significant savings in CPU time as compared to the low-Re approach, but standard wall functions employed in CFD software are based on empirically derived profiles of velocity, length scale, shear stress and turbulent kinetic energy, which are only applicable in very simple near-wall flows and can lead to major errors in complex, non-equilibrium flows.

In the most basic wall function, "universal" log-laws are adopted for the wall-parallel velocity and temperature, and values of the turbulence parameters are specified at the near-wall node, based on local-equilibrium assumptions. During the 1970's and 80's, a number of modifications to this treatment were suggested, to improve its performance in non-equilibrium flows. One of the first improvements, proposed by Launder & Spalding [1], was to replace the wall shear stress, τ_{wall}, in the velocity log-law with the turbulent kinetic energy, k (scaling the velocity with $k^{1/2}$ instead of the "friction velocity", $(\tau_{wall}/\rho)^{1/2}$, is crucial in flows involving separation, stagnation and reattachment, where the wall shear stress vanishes). The turbulent kinetic energy equation in the near-wall cell was solved with cell-averaged generation and dissipation rates, assuming constant shear stress and linear turbulence length scale variation ($k^{3/2}/\varepsilon \propto y$) across the near-wall cell. Chieng & Launder [2] proposed a wall function in which the near-wall cell was divided into two layers: the viscous sublayer and the fully turbulent region. In the viscous sublayer the shear stress, $\rho\overline{uv}$, was assumed to be zero and the turbulent kinetic energy to vary quadratically with wall distance, whilst in the fully turbulent region both $\rho\overline{uv}$ and k were assumed to vary linearly. Since at the wall the dissipation rate is given by $\varepsilon = 2\nu\left(\partial k^{1/2}/\partial y\right)^2$ and k varies quadratically, ε was assumed to take a uniform value in the viscous sublayer. In the fully turbulent region, ε was obtained from assuming an equilibrium turbulence length scale variation, $k^{3/2}/\varepsilon = c_l y$. The k-equation was solved in the near-wall cell using cell-averaged production and dissipation rates, and the dissipation rate, ε, was specified at the near-wall node. Johnson & Launder [3] modified this treatment, introducing a variable viscous sublayer thickness to account for changes in the near-wall shear stress distribution. More recently, Ciofalo & Collins [4] proposed making the sublayer thickness a function of the

local turbulence intensity. Two wall functions were proposed by Amano [5]. In the first, similar assumptions were adopted to the earlier treatments, but instead of only solving the k-equation in the near wall cell and prescribing the nodal value of ε based on local-equilibrium assumptions, Amano suggested solving transport equations for both k and ε in the near-wall cell using cell-averaged source and sink terms. The second wall function proposed by Amano used a three-layer model, in which different profiles for k and shear stress were used in the viscous sublayer, buffer layer and fully turbulent region. A recent proposal by Grotjans & Menter [6] assumed that the location of the wall, as specified by the user, was treated as the edge of the viscous sublayer to enable unlimited near-wall grid refinement.

All of the above-mentioned treatments rely upon an assumed semi-logarithmic velocity and temperature distribution in the near-wall cell. In an effort to move away from these restrictions, in the mid-eighties, attempts were made at slimming-down the storage requirement and computational cost of the low-Reynolds-number modelling approach by assuming a constant static pressure distribution in a thin layer adjacent to the wall - the parabolic sublayer (PSL) [7]. In this treatment, the pressure-correction algorithm was not solved in the near-wall cells and the wall-normal velocity was instead obtained directly from continuity, reducing the storage requirement and improving the convergence rate. The PSL approach, however, encountered difficulties in complex geometries with the calculation of velocity in corner cells.

Efforts at UMIST have recently been focussed on two novel and independent wall treatments. One of these is based on the analytical integration of the momentum and energy equations, accounting for the effects of convection, pressure gradient and buoyancy forces [8]. Inevitably fairly simple prescriptions of turbulent viscosity had to be made to allow an analytical integration. The second, described below, is based on the efficient one-dimensional numerical integration of simplified low-Re model equations in the near-wall cell.

Section 2 below explains the assumptions adopted and some implementation issues associated with the numerical wall function. In Section 3, results are presented from applying the new wall function to a fully-developed channel flow, using a 2-D elliptic flow solver, and an axisymmetric impinging jet. Comparisons are drawn between a standard wall function, the new wall function and low-Re model predictions. Computational costs of these various treatments are also presented.

2 SUBGRID WALL FUNCTION

The wall-function strategy presented here employs a grid similar to that used with a standard high-Re treatment (with a large near-wall cell) and calculates values for similar source terms to those approximated in standard treatments (such as wall shear stress, τ_{wall}, average production, $\overline{P_k}$, and average dissipation, $\overline{\varepsilon}$). However, instead of assuming profiles of velocity and length scale, the profiles of the mean flow and turbulence parameters across the near-wall control volume are obtained from solving simplified boundary-layer-type

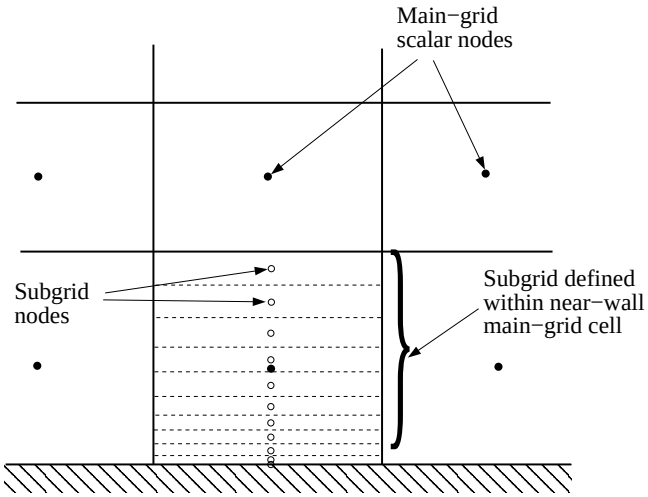

Figure 1: Subgrid arrangement within the near-wall main-grid control volume

transport equations using a fine subgrid spanning the wall-adjacent control volume.

The subgrid wall function differs from standard low-Re treatments in that it decouples the numerical solution of the near-wall region from that of the main region of the flow domain and also because it does not involve the solution of the pressure correction equation over the subgrid. Since, effectively, 1-D boundary-layer equations are solved in the subgrid for each near-wall control volume along the wall, the new wall function does not suffer from the slow convergence problems of a low-Re calculation.

The subgrid wall function has been developed within the framework of the finite-volume elliptic code, TEAM [9], which employs a structured, fully-staggered, Cartesian grid. Scalar quantities, including pressure, are stored at main-grid nodes in the centre of cells, shown in Figure 1, whilst velocities are stored at cell faces. The subgrid wall function could, however, equally be applied with other grid arrangements.

2.1 Governing Equations

A number of assumptions are applied within the subgrid in order to obtain a simplified set of transport equations: only the momentum equation(s) parallel to the wall are solved, the diffusion parallel to the wall is assumed to be negligible in comparison to that normal to the wall, and the pressure gradient is assumed to be constant across the near-wall main-grid cell. The simplified low-Re transport equations solved in the subgrid, in 2-D Cartesian coordinates, are then as follows:

- Wall-parallel U-momentum

$$\rho U\frac{\partial U}{\partial x}+\rho V\frac{\partial U}{\partial y}=-\frac{\partial P}{\partial x}+\frac{\partial}{\partial y}\left(\mu\frac{\partial U}{\partial y}-\rho\overline{uv}\right) \tag{1}$$

- Turbulent kinetic energy, k

$$\rho U\frac{\partial k}{\partial x}+\rho V\frac{\partial k}{\partial y}=\frac{\partial}{\partial y}\left[\left(\mu+\frac{\mu_t}{\sigma_k}\right)\frac{\partial k}{\partial y}\right]+\rho P_k-\rho\varepsilon \tag{2}$$

- Dissipation rate, $\tilde{\varepsilon}$

$$\rho U\frac{\partial \tilde{\varepsilon}}{\partial x}+\rho V\frac{\partial \tilde{\varepsilon}}{\partial y}=\frac{\partial}{\partial y}\left[\left(\mu+\frac{\mu_t}{\sigma_\varepsilon}\right)\frac{\partial \tilde{\varepsilon}}{\partial y}\right]+c_{\varepsilon 1}f_1\rho P_k\frac{\tilde{\varepsilon}}{k}-c_{\varepsilon 2}f_2\rho\frac{\tilde{\varepsilon}^2}{k}+\rho P_{\varepsilon 3}+\rho Y_c \tag{3}$$

- Temperature, T

$$\rho U\frac{\partial T}{\partial x}+\rho V\frac{\partial T}{\partial y}=\frac{\partial}{\partial y}\left[\left(\frac{\mu}{\sigma}+\frac{\mu_t}{\sigma_t}\right)\frac{\partial T}{\partial y}\right] \tag{4}$$

The production rate of turbulent kinetic energy, P_k is given by:

$$P_k=-\overline{uv}\left(\frac{\partial U}{\partial y}+\frac{\partial V}{\partial x}\right)-\overline{u^2}\frac{\partial U}{\partial x}-\overline{v^2}\frac{\partial V}{\partial y} \tag{5}$$

while the terms $P_{\varepsilon 3}$, and Y_c and the damping functions f_1 and f_2 are those associated with the particular low-Re model being used.

In the present work, the subgrid wall function has been tested with the linear $k-\varepsilon$ model of Launder & Sharma [10] and the cubic non-linear eddy-viscosity model (NLEVM) of Craft *et al.* [11] [12], although, in principle, any turbulence closure can be used. In the former model, the Reynolds shear stress, $\rho\overline{uv}$, is determined from:

$$\rho\overline{uv}=-\mu_t\left(\frac{\partial U}{\partial y}+\frac{\partial V}{\partial x}\right) \tag{6}$$

where the eddy-viscosity is given by:

$$\mu_t=c_\mu f_\mu\frac{k^2}{\tilde{\varepsilon}} \tag{7}$$

In the two-equation NLEVM of Craft *et al.*, additional quadratic and cubic functions of the strain-rate and vorticity are introduced in the anisotropy tensor, as follows:

$$\begin{aligned}
a_{ij}\equiv\frac{\overline{u_iu_j}}{k}-\frac{2}{3}\delta_{ij}= \;& -\frac{\nu_t}{k}S_{ij}+c_1\frac{\nu_t}{\tilde{\varepsilon}}\left(S_{ik}S_{kj}-\frac{1}{3}S_{kl}S_{kl}\delta_{ij}\right)\\
& +c_2\frac{\nu_t}{\tilde{\varepsilon}}\left(\Omega_{ik}S_{kj}+\Omega_{jk}S_{ki}\right)+c_3\frac{\nu_t}{\tilde{\varepsilon}}\left(\Omega_{ik}\Omega_{kj}-\frac{1}{3}\Omega_{lk}\Omega_{lk}\delta_{ij}\right)\\
& +c_4\frac{\nu_tk}{\tilde{\varepsilon}^2}\left(S_{ki}\Omega_{lj}+S_{kj}\Omega_{li}\right)S_{kl}\\
& +c_5\frac{\nu_tk}{\tilde{\varepsilon}^2}\left(\Omega_{il}\Omega_{lm}S_{mj}+S_{il}\Omega_{lm}\Omega_{mj}-\frac{2}{3}S_{lm}\Omega_{mn}\Omega_{nl}\delta_{ij}\right)\\
& +c_6\frac{\nu_tk}{\tilde{\varepsilon}^2}S_{ij}S_{kl}S_{kl}+c_7\frac{\nu_tk}{\tilde{\varepsilon}^2}S_{ij}\Omega_{kl}\Omega_{kl}
\end{aligned}$$

where the strain-rate and vorticity tensors are given by:

$$S_{ij} = \frac{\partial U_i}{\partial x_j} + \frac{\partial U_j}{\partial x_i} \qquad \Omega_{ij} = \frac{\partial U_i}{\partial x_j} - \frac{\partial U_j}{\partial x_i} \tag{8}$$

In addition to the above non-linear constitutive relation, the NLEVM also takes c_μ to be a function of invariants of the strain and vorticity tensors. In fact, where the near-wall flow resembles a shear flow, it is this functional form of c_μ which makes the larger contribution to the improved predictions of the subgrid shear stress. However, the non-linear stress-strain relation does improve the normal stress distribution and hence leads to a better representation of the near-wall turbulence energy production, P_k, in flow regions such as impingement zones.

The so-called "Yap correction", Y_c, is included in the $\tilde{\varepsilon}$-equation to reduce the turbulence length-scale in regions of flow separation and impingement. The standard Yap correction [13], used with the Launder-Sharma scheme, requires the specification of the wall-normal distance which can be difficult to prescribe in complex flows. A differential form of Yap correction, introduced by Iacovides & Raisee [14], is used with the NLEVM, which removes the explicit use of the wall-normal distance by using gradients of the turbulence length scale.

The low-Reynolds-number NLEVM of Craft *et al.* has previously been shown to perform well in a wide variety of flows, including flow in straight and curved channels, rotating pipes, flow over a turbine blade [15] and, more recently, impinging jet flows and abrupt pipe expansions [12].

2.2 Implementation of the Subgrid Wall Function

Subgrid convection is modelled in non-conservative form, as shown above (equations 1-4) since, in an isothermal situation where there is no wall heating, the conservative form of the convection term can lead to a non-zero source/sink term in the subgrid temperature equation, due to mass flux imbalance through the cell faces. Convection parallel to the wall is calculated using neighbouring subgrid values, requiring storage of the transported quantities (U, k, $\tilde{\varepsilon}$ and T) in each subgrid along the length of the wall.

Convection normal to the wall uses a wall-normal V-velocity calculated via continuity across the subgrid, as in a conventional boundary-layer procedure: the subgrid V-velocity is calculated sequentially from the wall-adjacent subgrid cell, which has a prescribed flux through the wall surface (zero in the case of an impermeable wall), to the outer edge of the subgrid. This wall-normal velocity, calculated from subgrid continuity, is then scaled to ensure that the subgrid velocity at the outer boundary (shown as position n in Figure 2) matches the main-grid velocity at that location. Although continuity is not rigorously satisfied in the subgrid cells due to this scaling, it is necessary to ensure consistent velocity boundary conditions. Subgrid convective terms are discretized using an upwind scheme.

The pressure gradient ($\partial P/\partial x$) is calculated from interpolated main-grid e and w values of P (see Figure 2) and this value is assumed to apply for all subgrid cells. Boundary

conditions at the wall are the same as those used in low-Re calculations. The boundary conditions at the northern boundary are determined from linear interpolation of main-grid nodal values at N and P.

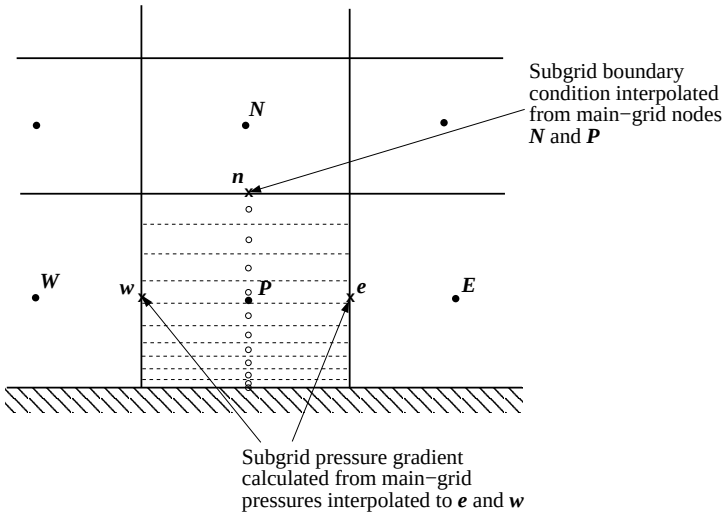

Figure 2: Subgrid arrangement showing calculation of boundary conditions and pressure gradient

Coding of the subgrid transport equations is relatively straightforward, with each equation integrated and discretized using the finite-volume method as in simple one-dimensional diffusion problems (see, for instance, Versteeg & Malalasekera [16]). The subgrid transport equations can be written in the general form:

$$\rho U \frac{\partial \phi}{\partial x} + \rho V \frac{\partial \phi}{\partial y} = \frac{\partial}{\partial y}\left(\Gamma \frac{\partial \phi}{\partial y}\right) + S \tag{9}$$

where ϕ denotes U, k, ε or T. Integrating this equation across a subgrid cell and re-arranging it in terms of coefficients of subgrid nodal values, one obtains the following discretized equation:

$$a_P \phi_P = a_N \phi_N + a_S \phi_S + S \tag{10}$$

Here the source term, S, can be expressed as:

$$S = s_P \phi_P + s_U \tag{11}$$

Negative sources in the subgrid k and $\tilde{\varepsilon}$ equations are included in source s_P which can be incorporated into the left-hand-side of equation 10. This increases the magnitude of a_P and improves the stability of the solution by increasing the diagonal dominance of the coefficient matrix. All other sources, including the wall-parallel pressure gradient in the momentum equation, are included in s_U. In a similar manner, terms resulting from convection parallel to the wall are split between sources s_U and s_P depending on their

sign. Convection normal to the wall is treated implicitly and results in additional terms in s_P, a_N and a_S. A summary of the convective terms appearing in the discretized subgrid transport equations is given below:

$$s_U = \frac{max\left(U_P, 0\right)\rho\phi_W}{\Delta x_{PW}}\Delta V_{cv} + \frac{max\left(-U_P, 0\right)\rho\phi_E}{\Delta x_{EP}}\Delta V_{cv} \tag{12}$$

$$\begin{aligned} s_P \;=\; & \frac{min\left(-U_P, 0\right)\rho}{\Delta x_{PW}}\Delta V_{cv} + \frac{min\left(U_P, 0\right)\rho}{\Delta x_{EP}}\Delta V_{cv} \\ & + \frac{min\left(-\rho V_P, 0\right)}{\Delta y_{PS}}\Delta V_{cv} + \frac{min\left(\rho V_P, 0\right)}{\Delta y_{NP}}\Delta V_{cv} \end{aligned} \tag{13}$$

$$a_N = \frac{max\left(-\rho V_P, 0\right)}{\Delta y_{NP}}\Delta V_{cv} \qquad a_S = \frac{max\left(\rho V_P, 0\right)}{\Delta y_{PS}}\Delta V_{cv} \tag{14}$$

where ΔV_{cv} is the subgrid cell volume and Δx and Δy distances are shown in Figure 3. The proliferation of max and min terms in equations 12 to 14 is due to the upwind scheme being employed for subgrid convection.

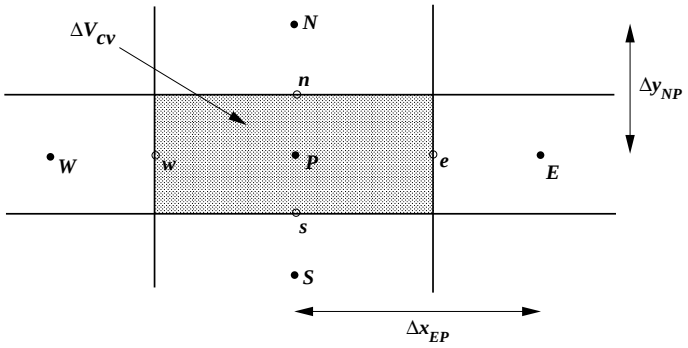

Figure 3: Subgrid node notation

A small amount of under-relaxation is required for the subgrid k and $\tilde{\varepsilon}$ equations (with typical under-relaxation factors of 0.9), whilst the subgrid momentum and temperature equations require no under-relaxation.

The discretized subgrid transport equations are solved using a tri-diagonal matrix algorithm (TDMA). One sweep of the subgrid TDMA is performed for each main-grid iteration, so the subgrid solution converges as the main-grid solution converges. Following each subgrid iteration, wall-function parameters are calculated: wall shear stress, average source and sink terms in the k and $\tilde{\varepsilon}$ equations ($\overline{P_k}$, $\overline{\varepsilon}$, $\overline{P_k\tilde{\varepsilon}/k}$, $\overline{f_2\tilde{\varepsilon}^2/k}$, $\overline{P_{\varepsilon 3}}$ and $\overline{Y_c}$), and wall temperature, T_{wall}, or wall heat flux, q_{wall}. These wall-function parameters are then applied as source terms in the main-grid wall-adjacent cells following the conventional

wall-function approach. Low-Reynolds-number terms are included in the equations solved in the main-grid, so that arbitrarily small near-wall cell sizes can be used.

The subgrid nodes are placed within the near-wall cell and increase in distance from the wall according to a simple geometric expansion. The number and distribution of these nodes needs to be adjusted for each case studied, to ensure that results are independent of the subgrid node density.

The coding of the subgrid wall function was initially validated by reconfiguring it as a simple 1-D parabolic channel flow solver. Results obtained using the wall function in this manner were identical to those obtained using the 2-D low-Reynolds-number TEAM code (see below).

3 APPLICATIONS OF WALL FUNCTIONS

3.1 Channel Flow

The new wall function was first applied to a simple 2-D fully-developed channel flow with periodic inlet and outlet boundaries and Reynolds number, based on bulk velocity and channel width (wall to wall), of $100,000$. The results obtained using two different near-wall main-grid cell sizes are shown in Figures 4 and 5, corresponding to near-wall nodal y^+ values of approximately 30 and 80. Both subgrid wall function and Low-Re results were obtained using the Launder & Sharma $k-\varepsilon$ model [10].

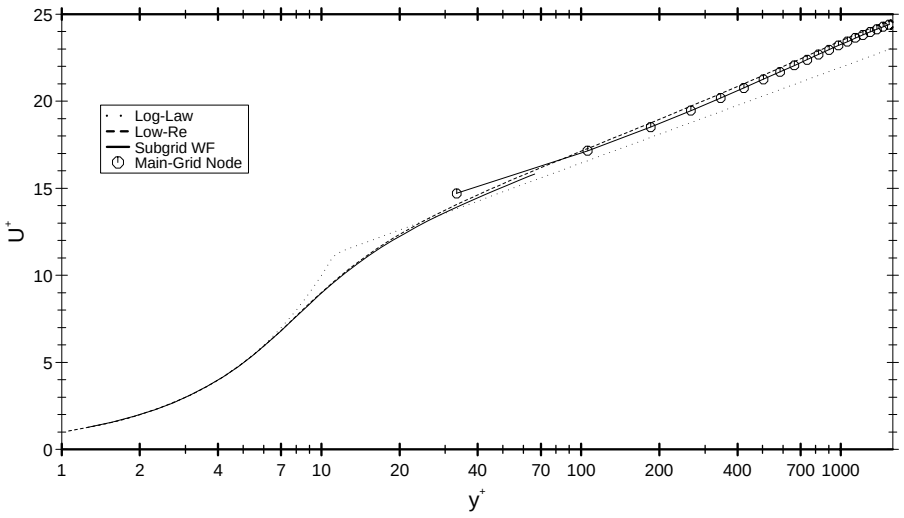

Figure 4: Subgrid wall function velocity log-law with $y^+ \approx 30$

The subgrid wall function results for the channel flow are in good agreement with the low-Re results for both near-wall cell sizes. A small discrepancy in the near-wall main-grid nodal velocity is due to the linear interpolation between the two near-wall nodes, used to obtain the subgrid boundary condition. Several other methods of interpolating

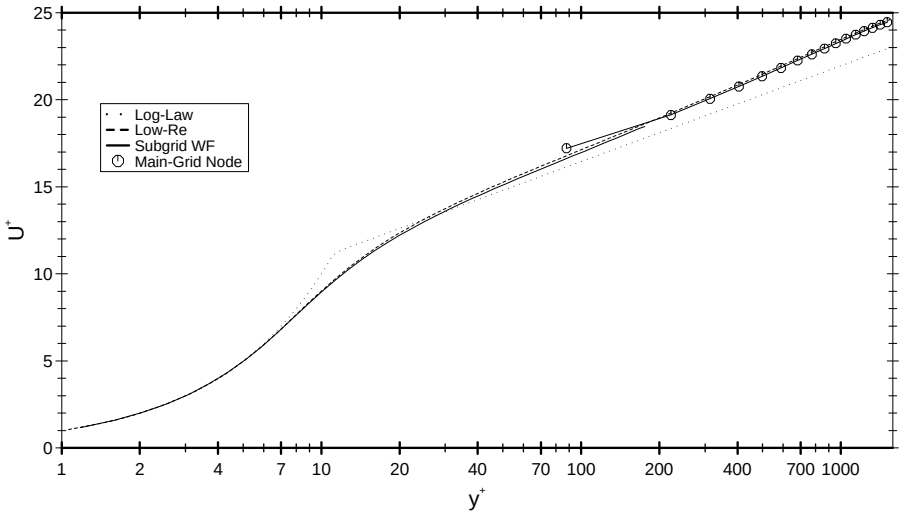

Figure 5: Subgrid wall function velocity log-law with $y^+ \approx 80$

have been tested for the subgrid boundary condition, but none provided any significant improvements without diminishing the generality of the wall function. In any case, within the near-wall cell the subgrid solution provides a more accurate prediction of the velocity profile and this can be used to gain a better picture of the velocity close to the wall if necessary. The results also show little dependence upon the size of the near-wall main-grid cell.

3.2 Axisymmetric Impinging Jet

There have been several previous numerical simulations and experimental studies of the impinging jet, reflecting the range of related industrial flows and the usefulness of this particular geometry for testing turbulence models. Jet impingement causes high levels of heat transfer rates near the stagnation point and is used in industrial applications where heating, cooling or drying processes are required. As a test case, the impinging jet offers insight into the behaviour of turbulence models in flow regimes far removed from the traditional simple shear flow. In an axisymmetric impinging jet, there is significant irrotational straining near the stagnation point, and near the edge of the impinging jet there is strong streamline curvature. Moving further downstream, the flow tends towards a simple radial wall jet in which the maximum shear stress occurs outside the wall region. Turbulence models and wall functions are often developed with reference to flows parallel to walls where none of these features occur.

There have been a number of previous numerical simulations of impinging jet flows using wall functions. Heyerichs & Pollard [17] compared the performance of six low-Reynolds-number near-wall closures and three wall functions, including the Chieng & Launder wall function. No definitive conclusions about the superior performance of any

one of the wall functions was made, except for the general comment that wall functions are unsuitable for complex flows where the assumptions used in their derivation are not valid. Amano & Brandt [18] studied a range of impinging jet nozzle-to-plate distances, ranging from $2 - 40$ nozzle diameters, and Reynolds numbers from $50,000$ to $300,000$, and found, in general, that good agreement could be obtained between experimental and numerical predictions for the velocity, pressure and skin friction, using a linear $k-\varepsilon$ model with the Chieng & Launder wall function. This contrasts with the findings of Ashforth-Frost & Jambunathan [19] who found that for a confined impinging jet at a Reynolds number of $20,000$ and a nozzle-to-plate spacing of 2 jet diameters, the kinetic energy near the stagnation point was overpredicted by a factor of 9. They used the PHOENICS code with a linear $k - \varepsilon$ model and a wall function based on the velocity log-law and local-equilibrium assumptions. The poor performance of the numerical simulation in the stagnation region was attributed to both the isotropic linear eddy-viscosity model and the wall function. Bouainouche *et al.* [20] evaluated the performance of a simple wall function, based on the velocity log-law and prescribed nodal values for k and ε, and a "generalized" wall function in which a simplified transport equation for k was solved in the near-wall cell with cell-averaged production and dissipation rate source terms. Both approaches were shown to have shortcomings in the prediction of wall shear stress for impinging jet flows, although the latter model showed a lower sensitivity to changes in the near-wall grid spacing. A hybrid wall function was proposed which switched from the generalized wall function, used in the impingement zone, to the simple wall function, used downstream, at an *ad hoc* prescribed radial distance.

In the present study, heat transfer predictions obtained using the subgrid wall function are compared to those obtained from the Chieng & Launder wall function and low-Reynolds-number model results, using the linear $k - \varepsilon$ model of Launder & Sharma [10] and the non-linear $k - \varepsilon$ model of Craft *et al.* [12]. The Chieng & Launder wall function was chosen for comparison following a study which showed that it out-performed other simple wall functions in impinging flows [21], in agreement with an earlier study by Amano & Jensen [22].

The impinging jet geometry studied here is one of those examined experimentally by Baughn *et al.* [23] and Cooper *et al.* [24] with a jet discharge height to diameter ratio, $H/D = 4$, and Reynolds number, based on the inlet pipe diameter and bulk velocity, of $70,000$. The flow domain dimensions and boundary conditions are shown in Figure 6. Previous studies [19] have noted that the entrainment boundary at the edge of the jet can sometimes lead to numerical instabilities. In the present study this was overcome by including a short length of pipe (one half a jet diameter in length) at the jet inlet, within the computational domain.

For the low-Reynolds-number model a grid of 90×70 (axial$\times$radial) nodes was used to examine the impinging jet (see Figure 7) in which cells were strongly clustered towards the wall, with maximum near-wall node values of y^* less than 0.5 and ten nodes within $y^* \leq 30$. An increase in the node density to 120×90 nodes showed a difference of

only 2 percent in the Nusselt number, limited to the region near the stagnation point ($r/D < 0.3$). The low-Re results obtained using the 90×70 grid were thus considered adequately grid-independent.

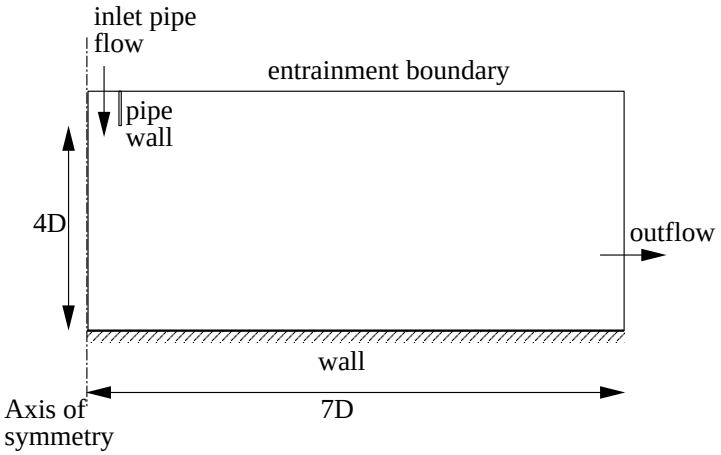

Figure 6: Impinging jet flow domain and boundary conditions

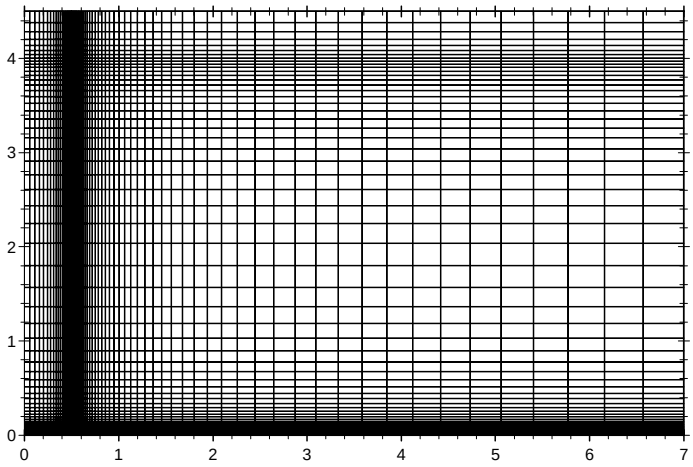

Figure 7: Low-Reynolds-number 90×70 grid

The wall-function grids used in this study had an identical distribution of nodes to the low-Re grid in the radial direction. In the axial direction, 45 nodes were used, with some clustering towards the wall and near the pipe entrance, as shown in Figure 8. To determine the effects of changing the near-wall cell size, four different near-wall cell sizes were tested, corresponding to y^* values varying in the range $310 \leq y^* \leq 620$ at the stagnation point and $60 \leq y^* \leq 150$ at $r/D = 6$. In the Nusselt number comparisons given later (Figures 9 and 10), these four cell sizes are denoted by $DX = 250$, 300, 400 and

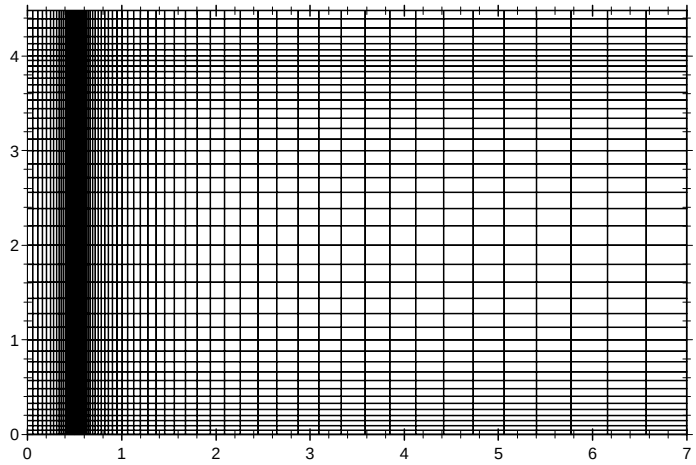

Figure 8: High-Reynolds-number 45 × 70 grid

500. The smallest of these cells ($DX = 250$) was identical in thickness to the neighbouring cell (one cell removed from the wall), whilst the others resulted in near-wall cells larger than the neighbouring cell. The actual value of DX represents the ratio of the physical width of the near-wall cell to that used in the the low-Reynolds-number grid.

In both the low-Re and high-Re computations, convective transport of momentum and temperature was approximated using the third-order quadratic upwind scheme, QUICK [25], whilst power-law differencing, PLDS [26], was used for turbulence parameters. At the pipe inlet, a fully-developed pipe flow was applied, which was obtained separately from a parabolic solver (as in Craft *et al.* [27]). Over the upper entrainment boundary (shown in Figure 6) a uniform static pressure was applied and velocity was obtained from continuity. If the flow was leaving the domain, zero-gradient conditions were applied for the turbulence parameters, whilst if the fluid was entering the domain k and ε were assigned small but finite values. Along the outlet boundary, zero gradient conditions were applied for pressure and turbulence parameters. The velocity parallel to the plane of the outflow boundary was set to zero and the radial velocity was calculated from $\partial\left(rU\right)/\partial r = 0$. On the axis of symmetry, zero-gradient conditions were adopted for all quantities except for the velocity component normal to the axis which was set to zero.

In the low-Re model, along the wall, turbulence parameters were set to zero ($k = \tilde{\varepsilon} = 0$) and the no-slip condition was applied for the wall-parallel velocity. A constant heat flux condition was applied along the wall, in agreement with the experiments, and the wall temperature was determined from Fourier's law. The Chieng & Launder wall function [2] was of the same form as that described in Section 1 with, in addition, contributions from the normal stresses in the cell-averaged production rate, $\overline{P_k}$. This has previously been shown to improve the turbulent kinetic energy prediction in the stagnation region of impinging flows [21].

The subgrid wall function applied to the impinging jet was identical to that proposed

in Section 2 with the exception that axisymmetric terms were included in the transport equations and in the turbulent kinetic energy production term. For each of the near-wall cell sizes tested, care was taken to ensure that the subgrid wall-function predictions were independent of the subgrid node density. Typically this involved 40 subgrid nodes with an algebraic expansion ratio of 1.08.

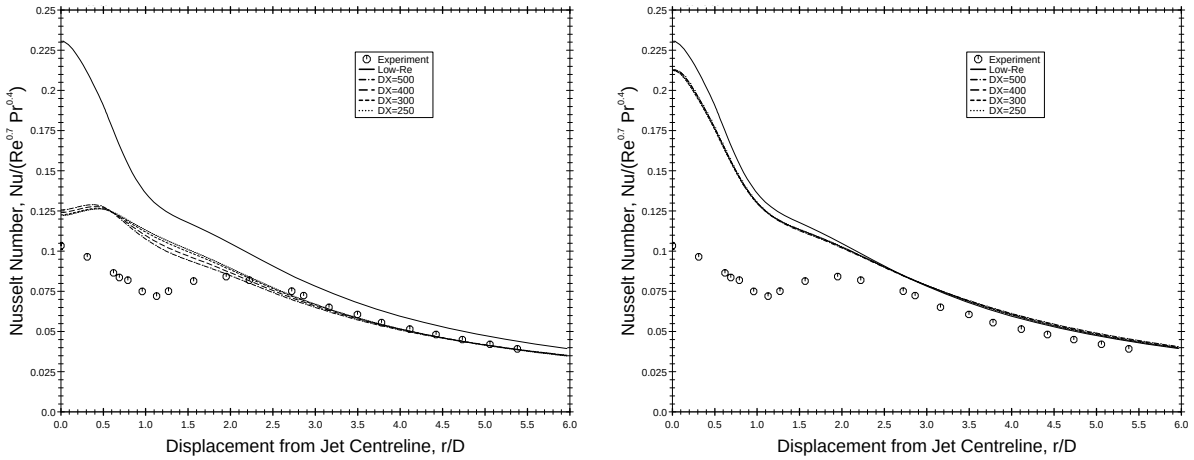

Figure 9: Nusselt number predictions for the impinging jet ($H/D = 4$, $Re = 70,000$) using the linear $k-\varepsilon$ model; broken lines are wall function results with different near-wall cell sizes; *a.*) Chieng & Launder wall function; *b.*) subgrid wall function

Nusselt number predictions for the axisymmetric impinging jet are shown in Figures 9 and 10. The first two graphs were obtained using the Launder & Sharma $k-\varepsilon$ model with either the Chieng & Launder wall function (Figure 9*a*) or with the subgrid wall function (Figure 9*b*). In each case, dotted lines represent wall-function results for a range of near-wall cell sizes corresponding to y^* values varying approximately in the range $310 \leq y^* \leq 620$ at the stagnation point and $60 \leq y^* \leq 150$ at $r/D = 6$. The graphs also show experimental Nusselt number results, taken from Baughn *et al.*, and low-Re model predictions.

The subgrid wall function shows good agreement with the low-Re model predictions when a linear model is used (Figure 9*b*). The slightly lower value of Nu near the stagnation point was due to an insufficient resolution of the peak in k, which occurs outside the near-wall main-grid cell. An increase in the number of main-grid nodes in this region (whilst maintaining the same near-wall cell size) brings the subgrid wall-function predictions closer to the low-Re result. The Chieng & Launder wall function, in contrast, does not capture the strong rise in Nu towards the stagnation point and shows overall Nu levels that, although closer to the experimental values, are in poor agreement with the low-Re model.

It is well known that any linear eddy-viscosity model overpredicts k, and hence the heat transfer coefficient, in regions of flow impingement, even with the Yap correction

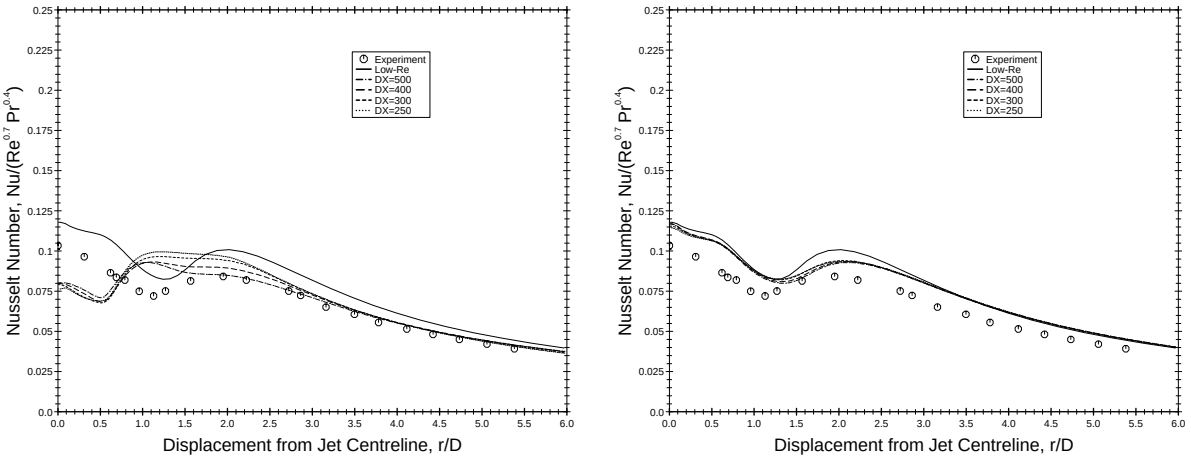

Figure 10: Nusselt number predictions for the impinging jet ($H/D = 4$, $Re = 70,000$) using the non-linear $k-\varepsilon$ model; broken lines are wall-function results with different near-wall cell sizes; *a.*) Chieng & Launder wall function; *b.*) subgrid wall function

[27]. The low-Re non-linear $k-\varepsilon$ model of Craft *et al.*, however, shows overall Nusselt number levels in closer agreement with the experimental values (see Figure 10). The Chieng & Launder wall function with the NLEVM (Figure 10*a*) incorrectly predicts the maximum heat transfer at $r/D = 1$ and underpredicts the stagnation Nusselt number, returning values 36% lower than the low-Reynolds-number solution. In contrast, the subgrid wall function with the NLEVM (Figure 10*b*) shows good agreement with the low-Re model predictions, with a maximum discrepancy of 8 percent at $r/D = 2$. With both linear and non-linear turbulence models, the subgrid wall function shows negligible sensitivity to changes in the size of the near-wall control volume, whilst the Chieng & Launder model shows differences of up to 14 percent.

Figures 11*a* and 11*b* show the resultant velocity profiles, $(U^2 + V^2)^{1/2}$, from the Chieng & Launder wall function and the subgrid wall function using the NLEVM in the impinging jet at a radial position, $r/D = 0.5$. Solid lines indicate the wall-function predictions with a near-wall cell size $DX = 250$, with circles marking the main-grid nodes. Experimental values are taken from Cooper *et al.* [24]. Both the Chieng & Launder and the subgrid wall function resultant velocity profiles appear to agree well with the low-Re results, with the subgrid wall function velocity showing slightly better agreement between y/D of 0.1 and 0.2. Both low-Re and wall-function treatments lead to smaller predicted velocities than measured by between 5 and 15 percent.

Semi-logarithmic plots of the normalized radial velocity at the same location ($r/D = 0.5$) show the difference between the Chieng & Launder and the subgrid wall functions more clearly. Figure 12*a* shows the velocity variation for the Chieng & Launder wall function compared to the low-Re result and the "universal" log-law. Circles mark the main-grid nodal values and since the log-law is imposed in the Chieng & Launder wall

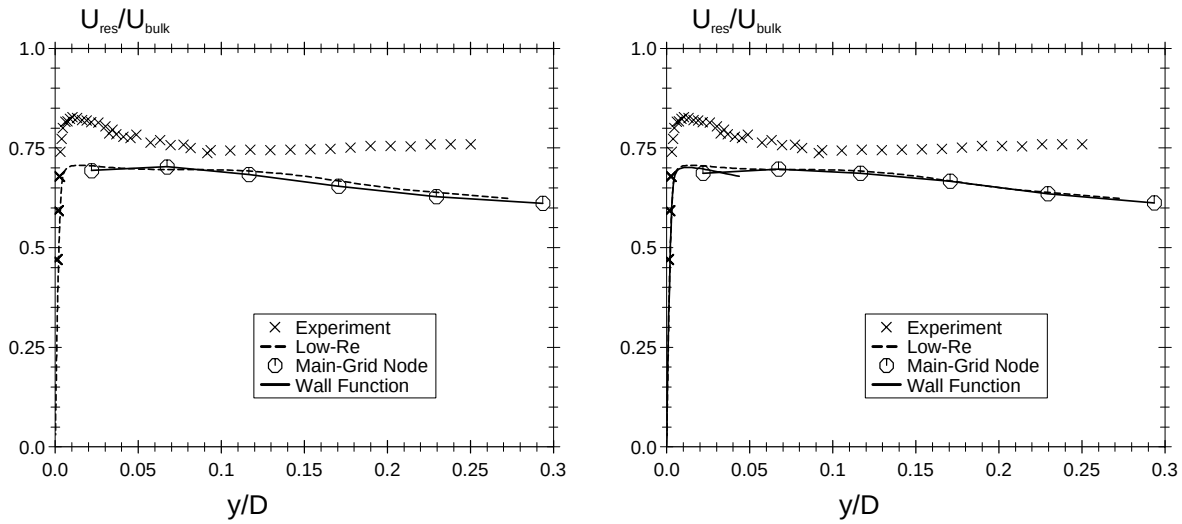

Figure 11: Resultant velocity profiles for the impinging jet ($H/D = 4$, $Re = 70,000$) at $r/D = 0.5$ with the non-linear $k - \varepsilon$ model; *a.*) Chieng & Launder wall function; *b.*) subgrid wall function

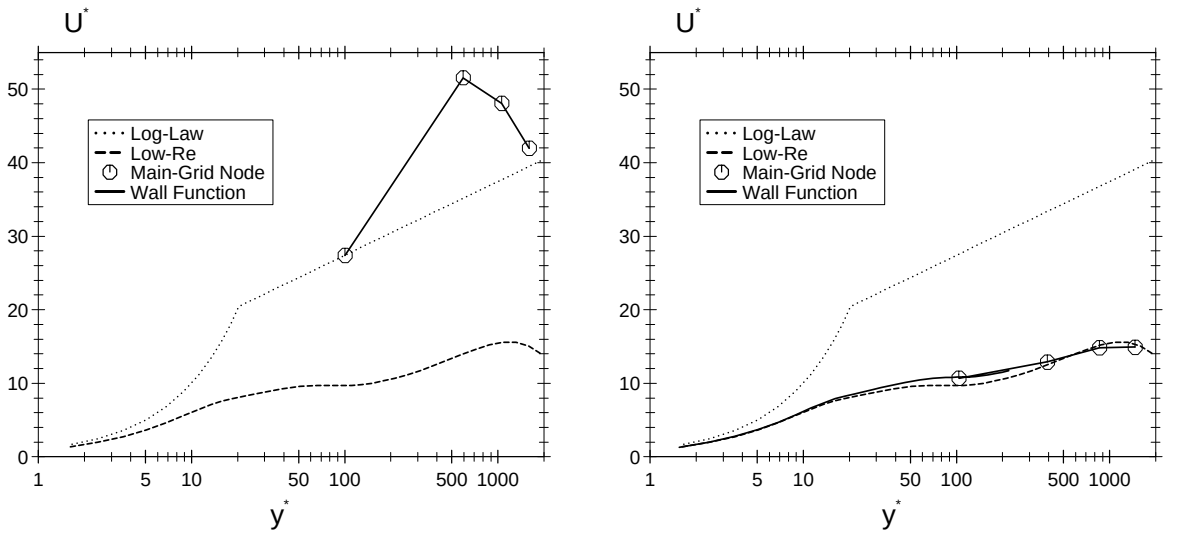

Figure 12: Plots of the wall-parallel velocity for the impinging jet ($H/D = 4$, $Re = 70,000$) at $r/D = 0.5$ with the non-linear $k - \varepsilon$ model *a.*) Chieng & Launder wall function; *b.*) subgrid wall function

function, the circle representing the near-wall node falls on the dotted universal log-law line. In this region in the impinging flow, the radial velocity is undergoing strong acceleration and the log-law is clearly inapplicable. Indeed, the near-wall dimensionless velocity, U^*, predicted by the Chieng & Launder wall function is more than twice that predicted by the low-Re model. In contrast, the subgrid wall-function predictions, shown in Figure 12b, are in excellent agreement with the low-Re results, with a difference of only a few percent. The differences between the Chieng & Launder and the subgrid wall function are more visible on the semi-logarithmic plots than with the linear-axes primarily because of the turbulent kinetic energy scaling used to obtain values of U^* and y^*.

Tables 1 and 2 show comparisons of CPU costs for the axisymmetric impinging jet computations using the linear and non-linear $k-\varepsilon$ models respectively. Calculations were run on a Silicon Graphics O_2 workstation with the same levels of under-relaxation and compiler optimization in each case. The subgrid wall function required 40 subgrid nodes in order for the solution to become grid-independent.

	Wall Functions		**Low-Re**
	Chieng & Launder	**Subgrid**	**Launder & Sharma**
Number of Nodes	70×45	$70 \times 45(+40)$	70×90
CPU time per iteration (s)	0.147	0.228	0.270
No. of Iterations	1523	1392	9698
Total CPU Time (s)	224	318	2616
Relative CPU Time	**1**	**1.42**	**11.68**

Table 1: Computing times for the axisymmetric impinging jet using the linear $k-\varepsilon$ model

	Wall Functions		**Low-Re**
	Chieng & Launder	**Subgrid**	**Craft *et al.***
Number of Nodes	70×45	$70 \times 45(+40)$	70×90
CPU time per iteration (s)	0.158	0.260	0.324
No. of Iterations	1426	1380	9116
Total CPU Time (s)	226	359	2955
Relative CPU Time	**1**	**1.59**	**13.08**

Table 2: Computing times for the axisymmetric impinging jet using the Craft *et al.* NLEVM

While the new wall function requires up to 60% more computing time than a standard wall function, this is a small price to pay in return for the much greater accuracy of the prediction. Indeed, the predictions are very similar to those returned by the low-Reynolds-number NLEVM, but the computing time required is less than one-eighth of

the latter treatment. For flows involving multiple walls, a proportionally larger benefit seems likely to be achieved.

4 CONCLUDING REMARKS

The development of a new subgrid-based wall function has been presented and implementation issues have been discussed. The new treatment has exhibited superior performance to a standard wall function in impinging jet flows, achieving excellent agreement with results obtained using low-Reynolds-number models. The subgrid wall function leads to a modest increase in computing time of up to 60 percent compared to a standard wall function. This is, however, an order of magnitude less than a standard low-Reynolds-number treatment. Inevitably, the subgrid wall function requires greater storage than the standard wall function, roughly commensurate with that required by an equivalent low-Reynolds-number model calculation.

Future applications of this wall function will examine spinning-disc flows, in which the velocity skews significantly in the immediate vicinity of the wall (the region usually occupied by the high-Re near-wall cell). Standard wall functions are unable to capture such a skewing effect, and traditionally one has had to use a single or two-layer low-Re approach to predict such a feature. The new subgrid wall function should offer an accurate and economic alternative.

ACKNOWLEDGEMENTS

This work has been funded by the Engineering and Physical Sciences Research Council, through the ROPA scheme (grant reference GR/M99170), and the Models for Vehicle Aerodynamics (MOVA) EU-BRITE-EURAM Project (contract BRPR-CT98-0624).

Authors' names appear alphabetically.

REFERENCES

[1] B. E. Launder and D. B. Spalding. The numerical computation of turbulent flows. *Computer Methods in Applied Mechanics and Engineering*, 3:269–289, 1974.

[2] C. C. Chieng and B. E. Launder. On the calculation of turbulent heat transport downstream from an abrupt pipe expansion. *Numerical Heat Transfer*, 3:189–207, 1980.

[3] R.W. Johnson and B.E. Launder. Discussion of "On the calculation of turbulent heat transport downstream from an abrupt pipe expansion". *Numerical Heat Transfer, Technical Note*, 5:493–496, 1982.

[4] M. Ciofalo and M. W. Collins. k-ϵ predictions of heat transfer in turbulent recirculating flows using an improved wall treatment. *Numerical Heat Transfer*, B 15:21–47, 1989.

[5] R. S. Amano. Development of a turbulence near-wall model and its application to separated and reattached flows. *Numerical Heat Trensfer*, 7:59–75, 1984.

[6] H. Grotjans and F. R. Menter. Wall function for general application CFD codes. *ECCOMAS 98*, 1998.

[7] H. Iacovides and B. E. Launder. PSL - an economical approach to the numerical analysis of near-wall elliptic flows. *ASME J. Fluids Eng.*, 106:245, 1984.

[8] T. J. Craft, A. V. Gerasimov, H. Iacovides, and B. E. Launder. Progress in the generalization of wall-function treatments. In *Turbulent Heat Transfer III*, Alaska, 2001.

[9] P.G. Huang and M.A. Leschziner. *TEAM, an introduction and guide to the computer code.* Dept. of Mechanical Engineering, UMIST, 1984.

[10] B. E. Launder and B. I. Sharma. Application of the energy-dissipation model of turbulence to the calculation of flow near a spinning disc. *Lett. in Heat Mass Transfer*, 1:131–138, 1974.

[11] T. J. Craft, B. E. Launder, and K. Suga. Development and application of a cubic eddy-viscosity model of turbulence. *Int. J. Heat and Fluid Flow*, 17:108–115, 1996.

[12] T. J. Craft, H. Iacovides, and J. H. Yoon. Progress in the use of non-linear two-equation models in the computation of convective heat-transfer in impinging and separated flows. *Flow, Turbulence and Combustion*, 63:59–80, 1999.

[13] C.R. Yap. *Turbulent heat and momentum transfer in recirculating and impinging flows.* PhD thesis, Dept. of Mechanical Engineering, UMIST, 1987.

[14] H. Iacovides and M. Raisee. Computation of flow and heat transfer in 2-D rib roughened passages. *2nd Int. Symposium on Turbulence, Heat & Mass Transfer, Delft*, pages 21–29, 1997.

[15] K. Suga. *Development & application of a non-linear eddy viscosity model sensitized to stress and strain invariants.* PhD thesis, Dept. of Mechanical Engineering, UMIST, 1995.

[16] H. K. Versteeg and W. Malalasekera. *An introduction to computational fluid dynamics.* Longman Scientific & Technical, 1995.

[17] K. Heyerichs and A. Pollard. Heat transfer in separated and impinging turbulent flows. *Int. J. Heat Mass Transfer*, 39(12):2385–2400, 1996.

[18] R. S. Amano and H. Brandt. Numerical study of turbulent axisymmetric jets impinging on a flat plate and flowing into an axisymmetric cavity. *ASME Journal of Fluids Engineering*, 106(4):410–417, 1984.

[19] S. Ashforth-Frost and K. Jambunathan. Numerical prediction of semi-confined jet impingement and comparison with experimental data. *Int. J. Num. Meth. Fluids*, 23:295–306, 1996.

[20] M. Bouainouche, N. Bourabaa, and B. Desmet. Numerical study of the wall shear stress produced by the impingement of a plane turbulent jet on a plate. *Int. J. Num. Meth. Heat Fluid Flow*, 7(5-6):548–564, 1997.

[21] S. E. Gant. Assessment of wall function practices for impinging flows. First-Year PhD Report, Dept. of Mechanical Engineering, UMIST, Manchester, UK, 1999.

[22] R. S. Amano and M. K. Jensen. Turbulent heat transfer of impinging jet on a flat plate. In *ASME Paper No. 82-WA/HT-55, Winter Annual Meeting*, Phoenix, 1982.

[23] J. W. Baughn, X. J. Yan, and M. Mesbah. The effect of Reyolds number on the heat transfer distribution from a flat plate to a turbulent impinging jet. *ASME Winter Annual Meeting*, November 1992.

[24] D. Cooper, D. C. Jackson, B. E. Launder, and G. X. Liao. Impinging jet studies for turbulence model assessment: Part 1: Flow field experiments. *Int. J. Heat Mass Transfer*, 36(10):2675–2684, 1993.

[25] B. P. Leonard. A stable and accurate convective modelling procedure based on quadratic upstream interpolation. *Comput. Methods Appl. Mech. Eng.*, 19:59–98, 1979.

[26] S. V. Patankar. *Numerical heat transfer and fluid flow.* Series in Computational Methods in Mechanics and Thermal Sciences. Hemisphere Publ. Corp., McGraw-Hill, 1980.

[27] T. J. Craft, L. J. W. Graham, and B. E. Launder. Impinging jet studies for turbulence model assessment. part 2: An examination of the performance of four turbulence models. *Int. J. Heat Mass Transfer*, 36(10):2685–2697, 1993.